Characterization of the cathodic thermal behavior of molten $CaCl_2$ and its hygroscopic chloride mixture during electrolysis

Ryota Shibuya[1], Shungo Natsui[2,*], Hiroshi Nogami[2], Tatsuya Kikuchi[1] and Ryosuke O. Suzuki[1]

[1] Division of Materials Science and Engineering, Faculty of Engineering, Hokkaido University, Kita 13 Nishi 8, Kita-ku, Sapporo 060-8628, Japan

[2] Institute of Multidisciplinary Research for Advanced Materials, Tohoku University, Katahira 2-1-1, Aoba-ku, Sendai 980-8577, Japan

*Corresponding author. E-mail address: natsui@tohoku.ac.jp; Tel.: +81-22-217-5157

Abstract

A liquid metal electrochemically deposited in $CaCl_2$ or its chloride melts serves as an effective reductant for active metal oxides. Although a very low oxygen concentration can be achieved at a considerably high electrolysis efficiency, the existence of small amount of water impurity in molten chlorides, which is very difficult to detect, causes low electrolysis efficiency. In this study, to clarify the morphological and thermal characteristics of a cathodic electrode in a slightly hygroscopic LiCl–KCl–$CaCl_2$ melt, we simultaneously performed electrochemical measurements and thermal measurements using an ultrafine thermocouple inserted inside a Mo electrode (i.d. 1.57 mm).

Concomitantly, changes in the electrode interface were recorded at 500-μs intervals using a synchronized high-speed digital camera. Despite the small amount of water included in the system, the measured heat absorption was much smaller than thermodynamically predicted, which suggested that the generated hydrogen decreased the purity of the liquid alloy electrodeposited on the cathode surface possibly through hydride formation. By using the synchronized thermal measurement, it was possible to trace the change in the electrodeposition pattern of impurity water quickly and sensitively, which was difficult to determine in only the electrochemical potential-current response.

Keywords: Molten salt electrolysis; Thermal analysis; High-speed digital microscopy; Liquid metal electrodeposition; $CaCl_2$;

Graphical Abstract

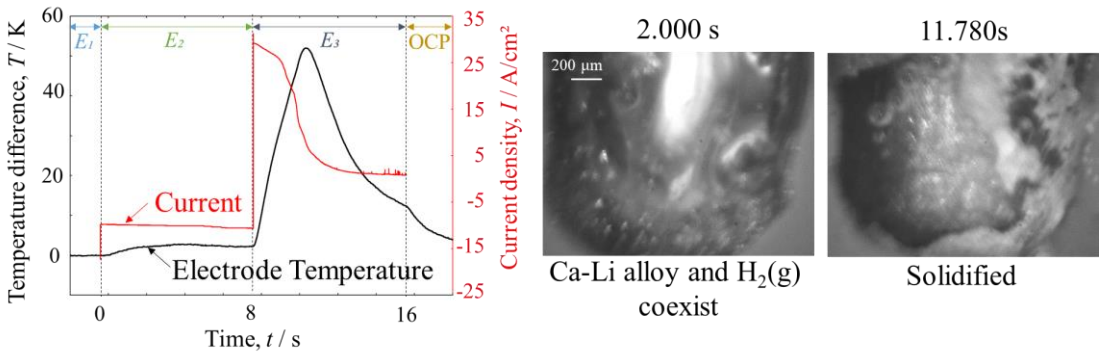

Introduction

The direct electrochemical reduction of active solid oxides XO_x (X = Ti, Zr, Hf, V, Nb, Ta, U, and other rare dispersed metals) is one of the important challenges for pyrometallurgical process. In the prevailing Kroll process for titanium production, which incurs an extremely high energy cost, TiO_2 must first be converted to $TiCl_4$ by Cl_2 gas, followed by use of liquid Mg as the reductant, and $MgCl_2$ as a by-product is circulated by electrolysis to give liquid Mg and gaseous Cl_2 [1]. As an alternative to this complex process, the direct decomposition of TiO_2 in molten $CaCl_2$ has received special attention because of its simplicity and low energy cost [2,3]. Higher productivity was expected through the "OS process," wherein oxide anion transfer in $CaCl_2$ is better utilized because as much as 20 mol% calcium oxide can dissolve in molten $CaCl_2$ at 1173 K [4,5]. In these methods, the solid TiO_2 placed in the vicinity of the cathode is reduced by metallic Ca in the salt bath, TiO_2 forms lower oxides [6], and finally, to metallic Ti via TiO formation [7].

The liquid Ca electrochemically deposited at the cathode also partially dissolves in the $CaCl_2$ melt, and the dissolved Ca effectively reduces the oxide. Similar to this mechanism, LiCl and its binary chloride systems can act at lower temperatures [8-10]. Moreover, the LiCl–$CaCl_2$ eutectic melt operates at a low temperature compared with single salts (KCl is occasionally added to further lower the temperature). Thus, it has attracted attention as a molten salt with high energy efficiency and high reducing properties [11-14]. As demonstrated above, metallothermic reduction in the OS process is performed by the dissolved metal (Me) in the vicinity of the cathode through the following reactions:

$$\mathrm{MeO} \rightarrow \mathrm{Me}^{2+} + \mathrm{O}^{2-} \quad (1)$$

$$\mathrm{Me}^{2+} + 2e^{-} \rightarrow \mathrm{Me\ (vicinity\ of\ the\ cathode)} \quad (2)$$

$$\mathrm{XO_x(s) + Me \rightarrow XO_{x-1}(s) + MeO} \quad (3)$$

The liquid Me effectively reduces XO_x even though the latter does not have any direct electrical contact with the cathode. Recently, this mechanism has been demonstrated to have more advanced application in the reduction system [15-19].

In this process, the theoretical residual oxygen in Ti must be 300 ppm O when Ca and calcium oxide coexisted in equilibrium at 1173 K [20]. This low oxygen level is suitable for industrial application. However, at present, the Ti obtained by electrolysis in molten salt contains at least 4000 ppm O [21]. One of the reasons for low electrolytic efficiency is the presence of a considerably low amount of impurity water in molten chlorides. In general, chlorides are highly hygroscopic and, thus, must be thoroughly dehydrated at high temperatures before use. Dehydration above 573 K is required to decompose $CaCl_2$ monohydrate, and dehydration at an elevated temperature as high as 873 K was effective in the same reaction vessel [7]. This dehydration achieves a low impurity water level that does not provide enough information about the potential-current response during electrolysis. However, a previous study indicated a pressure change that corresponds to water remaining in molten $CaCl_2$ even at 1050 K [21]. Although the hydrogen generated by the electrolysis of the water present in the molten salt possibly inhibits the reactions in eq. 1–3, details of its interaction with Me are unknown.

Although a clear understanding of the cathodic behavior in molten salt is necessary to control

and optimize the OS process, the transient behavior of the electrodeposition of liquid Me at the cathode is complicated because it depends on the morphology of liquid Me, including colloidal metal called "metal fog" [22-25]. In a previous study, we demonstrated that submillisecond high-speed microscopy synchronized with electrochemical measurement at submillimeter scale resolution is possible owing to advances in digital optical technology [26, 27]. Such knowledge can be immediately applied to current molten salt electrolytic processes to achieve energy saving from the viewpoint of thermal efficiency in the material industry. Furthermore, the simultaneous measurement of heat transfer characteristics [28-31] and observation of the reaction on the cathode surface will enable an understanding of the ongoing electrochemical and secondary reactions and nature and behavior of the melt in the presence of water impurity. In this study, to measure the temperature change of the cathode during molten salt electrolysis, a sensitive ultrafine thermocouple (TC) was inserted inside the electrode. Thus, thermal measurement of the thermoelectromotive analog signal was carried out simultaneously with electrochemical measurement. This procedure obtains similar information as the "hot-thermocouple method," which is widely used as a thermoanalytical scheme that includes visualization of the high-temperature melt reaction field [32-34]. In summary, this study determined the characteristics of the cathodic reaction in molten LiCl–KCl–$CaCl_2$ by examining images of the electrode surface obtained by high-speed digital microscopy, which was synchronized with the thermoanalytical and electrochemical measurements.

Experimental

A schematic diagram of the experimental apparatus is depicted in **Fig. 1**. All experiments were conducted using the following procedures.

Materials and electrochemical measurement conditions

Reagent-grade LiCl (>99.0 wt%), $CaCl_2$ (>95 wt%), and KCl (>99.5 wt%) (Wako Pure Chemical Industries Ltd.) were used to prepare molten salt. The impurities in each salt are mainly water, but also include Na (<200 ppm), Mg (<100 ppm), Sr (<100 ppm), SO_4 (<50 ppm), NO_3 (<30 ppm), Pb (<5 ppm), and Fe (<2 ppm). In this study, $CaCl_2$ melt (m.p. =1055 K), eutectic mixtures of LiCl–KCl–$CaCl_2$ (52:12:36 mol%, m.p. = 685 K), LiCl–$CaCl_2$ (65:35 mol%, m.p. = 748 K), and LiCl–KCl (59:41 mol%, m.p. = 625 K) were used. Each salt was placed in a borosilicate glass crucible with a flat surface and dried under approximately 2–3 Pa. A digital Pirani vacuum gauge (SW1, ULVAC, Inc.) was used to measure the in-furnace pressure. Each salt was then heated to the constant experimental temperature. All experiments were conducted under Ar atmosphere (>99.9995 vol.%). The melt temperature was measured using a K-type TC with a glass protection tube. After melting the mixed salt, the suspended electrodes were immersed in the melt while keeping the seal. Molybdenum was employed as the material of the working electrode (WE), which must be inert, resistant to high-temperature corrosion, and unreactive to the molten salt as well as the Ca and Li to be electrodeposited [35]. To measure the temperature of the WE, as shown in Fig. 1b, the TC was implanted in the WE, which was shaped into a thin tube (i.d.: 1.57 mm, >99.95%, surface polished with emery paper #1000,

Systembrain Co., Ltd.). The inserted ultrafine TC must be completely isolated from the circuit contributing to the electrochemical reaction for accurate temperature measurement. Because the Mo tube and implanted TC are insulated by MgO nanopowder, the temperature change due to the electrochemical reaction occurring on the Mo tube surface can be recorded. The immersion depth of the WE was fixed at 5 mm by using an insulated protective Al_2O_3 tube. The counter electrode was a graphite rod (i.d.: 10 mm, Toyo Carbon Corp.), and an Ag^+/Ag reference electrode was employed. An Ag^+/Ag reference electrode consisting of a silver wire (φ 1.0 mm, 99.99%, Nilaco) was immersed in the corresponding melt containing 0.5 mol% AgCl (Wako, 99.5%) and set in a quartz tube [13]. Electrochemical measurements were performed using an automatic polarization system (HZ-5000, Hokuto Denko Corp.).

Scheme for direct observation of the cathode

To elucidate the interfacial morphology of the WE, a quartz glass vessel (diameter: 100 mm, height: 250 mm, Kondo Science, Inc.) with a barrel-vaulted shape and flat surface for in situ observation was employed. An electric resistance furnace (SiC heater) was designed to control the inner vessel temperature for direct observation of processes within the vessel. A metal halide light (HVC-SL, Photron Co., Ltd., maximum light flux: 12,500 lm, main spectral peak: 550 nm) was used as an auxiliary light source. Changes in the electrode interface were recorded at a rate of 2000 fps (500-μs intervals), and a resolution of 640 × 480 pixels was obtained using a high-speed digital camera (HAS-D71, monochrome, main response spectral range: 500–600 nm, Ditect Co., Ltd.) and long-

distance zoom lens (VSZ-10100, working distance: 95 mm, VS Technology Co., Ltd.). The inter-electrode voltage and microscope images were synchronized with an error of 4 μs by using an analog signal synchronous system (DI-SYNC 29N, Ditect Co., Ltd.). The liquid-metal electrode interface was tracked in each captured image by using an image processing software (PFV Viewer, Photron Co., Ltd.).

Characterization of thermal behavior on WE

A "scopecorder" with a high noise-tolerant voltage measurement module (DL350 with 720254, Yokogawa Electric Co.) was used to measure the thermoelectromotive analog signal of the TC in the electrodes and bath, WE-counter electrode inter-electrode voltage for synchronization, and voltage signal output from the pressure gauge. The voltage measurement interval was constant at 100 μs. The minute thermoelectromotive force generated from TC was converted to a sharp waveform by an amplifier and a 10 Hz low-pass filter. Noise ingress from the environment was reduced by using a Bayonet Neill-Concelman cable for wiring.

Results and discussion

Cathodic thermal behavior of molten $CaCl_2$

The behavior of molten $CaCl_2$ single salt at 1173 K during constant potential electrolysis was investigated as a simple system. The chronoamperogram and synchronized temperature curve for molten $CaCl_2$ are shown in **Fig. 2**. To perform the best simultaneous in situ observation of the electrode

surface, the first holding potential (E_1) was set as the natural immersion potential, the second holding potential (E_2) was an arbitrary potential (from -1.6 to -2.7 V vs. Ag^+ / Ag, 2 s), the third holding potential (E_3) was the same as E_1 (2 s), and the final potential was the open circuit potential (OCP). The temperature obtained from the thermoelectromotive force temporal data of the TC inserted in the WE was analyzed differentially with the bath temperature measured by another TC. When $E = E_2$, the following reaction is considered:

$$\mathrm{Ca}^{2+} + 2\mathrm{e}^- = \mathrm{Ca} \quad (\mathrm{at}\, E = E_2) \tag{4}$$

The current increases as the applied potential becomes more negative, which indicates that the amount of precipitated Ca increases. At $-1.6 \leq E \leq -1.9$ V, temperature rises were observed only during $E = E_2$. At $-1.9 \leq E \leq -2.7$ V, the temperature tended to decrease. At this potential, the temperature decreases linearly with time, the temperature gradient increases, and the absolute temperature change increases as the applied potential becomes more negative. At $E = -2.6$ and -2.7 V, the temperature gradient changes from approximately t = 0.5 s. This change of heat transfer characteristics can be considered to be due to the shift of interfacial resistance. Near the equilibrium potential ($-1.8 \leq E \leq -1.6$ V), the deviation from the equilibrium potential is small, and Ohm's law can be applied to the electrode interface as “polarization resistance”. The ratio (overpotential, η)/(current density, i) corresponds to the resistance of the interface to the charge transfer reaction at the electrode-electrolyte interface; thus, if there is a large deviation from the equilibrium potential ($E < -1.8$ V), i becomes large and the polarization resistance is almost negligible [36]. **Fig. 3** presents

the time change through photographs of the WE surface. In the snapshots taken at different potentials, black metal fog was observed for the electrodeposited liquid Ca. The amount of deposited Ca increases when the applied potential becomes more negative, but the metal fog diffused offshore also increases. Thus, it is possible that the electrode temperature change also depends on the heat transfer characteristics of the vicinity of the WE.

Electrolysis of eutectic mixture

In this section, we focus the cathodic behavior during electrolysis of molten LiCl-KCl-$CaCl_2$ at lower temperature. **Figure 4a–d** shows the effect of changing E_2 on current-temperature-time curves, and **Fig. 5** shows the effect of changing the temperature at constant E_2 (-2.7 V). At $E = E_2$, all current values are almost constant, and the cathodic currents increase as the applied potential becomes more negative. This trend is similar to previously reported cyclic voltammograms [13, 14, 26, 27]. The electrochemical reactions at each potential are

$$\left.\begin{array}{c} \mathrm{Ca^{2+} + 2e^- \rightarrow Ca} \\ \mathrm{Li^+ + e^- \rightarrow Li} \\ x\mathrm{Ca} + y\mathrm{Li} \rightarrow x\mathrm{Ca}y\mathrm{Li} \end{array}\right\} \text{at } E = E_2 \qquad \begin{array}{l} \text{(5a)} \\ \text{(5b)} \\ \text{(5c)} \end{array}$$

$$x\mathrm{Ca}y\mathrm{Li} \rightarrow x\mathrm{Ca^{2+}} + y\mathrm{Li^+} + (2x + y)\mathrm{e^-}\} \text{ at } E = E_3 \qquad \begin{array}{l} \text{(6a)} \\ \text{(6b)} \end{array}$$

When E is kept constant as E_2, the trend in the magnitude of the steady cathode current density is (LiCl–$CaCl_2$) > (LiCl–KCl) > (LiCl–KCl–$CaCl_2$), i.e., LiCl–$CaCl_2$ has approximately twice the cathode current density of the other mixtures. On the other hand, at $E = E_3$, a large peak current corresponding to the dissolution of the electrodeposited metal is observed. Moreover, despite changing

E_2, the absolute current in each mixture is almost constant as 27, 25, and 15 A cm^{-2} for $LiCl–CaCl_2$, LiCl–KCl, and $LiCl–KCl–CaCl_2$, respectively. This is because the electrochemical dissolution rate of the electrodeposited metal is limited. According to previous reports [13,27], Ca-Li alloy is deposited in $LiCl–CaCl_2$ and $LiCl–KCl–CaCl_2$ and mainly Li in LiCl–KCl. This suggests that the dissolution rate of the electrodeposited Li is faster than that of Ca at $E = E_3$. Focusing on the temperature change of WE, a small temperature drop at $E = E_2$ and temperature rise at $E = E_3$ are observed in each mixture, and a larger calorific value is observed as potential becomes negative. The temperature drop is up to approximately -0.4 K, while the maximum temperature rise is 27 K. The trend in the maximum temperature at the same potential is ($LiCl–CaCl_2$) > ($LiCl–KCl–CaCl_2$) > (LiCl–KCl), which is not consistent with the trend in current density. Assuming that the magnitudes of the enthalpy change for electrochemical deposition and electrochemical dissolution of the Ca-Li alloy or Li are equal, the temperature change between E_2 and E_3 is expected to be balanced, contrary to observation. The recorded temperature of the WE at E_2 evidently includes the effect of another exothermic factor.

Figure 6 shows snapshots of the WE interface during the electrolysis of each mixture. The time period t <2.000 s corresponds to $E = E_2$, and a large number of shiny metallic Ca-Li alloy droplets are generated on the electrode surface and coalesce with the surroundings in $LiCl–KCl–CaCl_2$ and $LiCl–CaCl_2$. However, in LiCl–KCl, the behavior of Li droplets cannot be confirmed because a thick metal fog is generated in vicinity of the electrode. A previous report confirmed the formation of a metal fog with a hexagonal, network-like structure in $LiCl–CaCl_2$ [27]. In these mixtures, at t = 4.000 s,

bubbles are generated while the liquid droplets dissolve rapidly (see **Supplemental Movies 1** and **2** from the 14-s mark). If water is present in the molten salt bath, it is electrolyzed during the application of potential, thereby generating hydrogen. Therefore, removing water completely during the dehydration of the molten LiCl–KCl–$CaCl_2$ and LiCl–$CaCl_2$ baths is insufficient. For the reaction at $E = E_3$, one must consider not only hydrogen generation, but also the chemical reaction between the electrodeposited Ca-Li alloy and H_2 gas. Details of the latter are discussed in next section. In the case of LiCl–$CaCl_2$, some of the electrodeposited droplets solidify at $E = E_3$ and persist as a white solid. As the applied potential becomes negative, the amount of deposited solid increases. This white solid chemically dissolves in the molten salt while generating bubbles at E = OCP. On the other hand, in the case of LiCl–KCl, no solid (see **Supplemental Movie 3** from the 14-s mark) or bubbles are generated. Because LiCl–KCl is considered to be sufficiently dehydrated compared with other systems, water removal in $CaCl_2$ is expected to incomplete in this experiment, as previously reported [21].

Cathodic behavior in hydrogen coexistence system

In the lower temperature system, $CaCl_2$ was found to contain water even after dehydration and exhibited a remarkable electrode temperature rise during electrolysis. In this section, we discuss the mechanism of the electrochemical/chemical reaction at the cathode under the coexistence of hydrogen. **Figure 7** shows the potential dependence of the current efficiency, which is defined as the ratio between the electric charges passing through the amperograms. As the potential becomes negative, the current efficiency increases for all mixtures. The lower current efficiency can be attributed to

desorption from the electrode surface as a metal fog and hydrogen generation. Thus, when the potential is sufficiently negative, the electrochemical reaction rate of hydrogen generation is limited. In this case, we consider that metal deposition should be clearly observed.

Figure 8 shows the effect of applying a large negative potential (-3.0 V). When $E = E_2$, the temperature rises by about 2.5 K, and both the current density and temperature reach an almost steady state. Concurrently, the formation of metal droplets, metal fog, and bubbles on the electrode surface are observed from the microscope image. We found that after the bubbles are released from the electrode, they are absorbed again by the droplets on the electrode (see **Supplemental Movie 4**). In addition, when $E = E_3$, the anodic current is limited to approximately 30 A cm^{-2}, and a temperature increase of up to 52 K is recorded. Corresponding to this anodic current, solids are deposited on the electrode surface (t = 9.740 s) and bubbles are generated after the initial disappearance of droplets and diffusion of the metal fog around the electrode. As electrolysis proceeds, solids are dissolved in molten salt and discharge bubbles (t = 11.780 s). Although the current reaches approximately 0 A cm^{-2} at t >12 s at the end of potential application, these solids remain and continue to dissolve. Thus, chemical dissolution occurs without the transfer of electrons.

Since Ca-Li alloy and H_2(g) coexist, as shown in Fig. 8b (t = 2.0–8.0 s), there is a possibility that H_2(g) generation occurs by electrochemical reaction. Assuming that the bubbles are pure hydrogen generated from the hydroxide in molten salt [37], the following reactions of metal phase Me(= Ca, Li) are identified:

$$x\mathrm{Me(in\ liquid\ alloy)} + \mathrm{H_2} = x\mathrm{MeH_{(2/x)}} \quad (7)$$

$$\mathrm{MeH}_y + \mathrm{Me(OH)}_y\mathrm{(in\ salt)} = y\mathrm{Me_{(2/y)}O} + y\mathrm{H_2(g)} \quad (8)$$

These equations consider the possible reactions between the electrodeposited Ca-Li melt (approximate composition of the electrodeposited alloy was to be Ca: Li = 71: 29, according to ref. 27) and H_2. The deposited solids are believed to be hydrides or oxides. The formation of solid hydrides (m.p.: CaH_2 = 1089 K, LiH = 965 K) and solid oxides (m.p.: CaO = 2886 K, Li_2O = 1843 K) through reaction with moisture in molten salt should naturally proceed since the Gibbs free energy (ΔG) values of these reactions are negative according to a chemical equilibrium calculation software (FactSage7.0). Here, the molten salt chemically dissolves the oxide [3], as shown in Fig. 8b) (t = 11.780 s). Like the previously proposed mechanism, H_2(g) is generated without the transfer of electrons for LiCl-based molten salt electrolysis[38]. These are natural mechanisms, considering that hydride has a low electrical conductivity and will not be electrodeposited.

Consideration of metal fog morphological effect by thermal characterization

The macroscopic energy balance during the electrochemical reaction may have changed with the applied potential due to formation of metastable metal fog: the excess energy was probably required to create the dispersed metal-and-salt interface, and this energy depends on the microscopic fog morphology [39, 40]. In this section, we analyzed the thermal behavior data obtained in Section 3.1 to consider the effect of the morphology of the electrodeposited Ca in molten $CaCl_2$, as shown in Eq. 4.

The heat balance of the WE surface was evaluated in order to characterize the heat transfer at

each potential. The thermal behavior accompanying the electrochemical reaction has been described in previous studies [28-31, 41-43]. Here, we will briefly describe our interpretation. First, when the temperature T and the pressure P are constant and the chemical reaction proceeds, according to the first law of thermodynamics, the internal energy ΔU and the heat absorbed by the reaction system Q are expressed as $\Delta U = T\Delta S - (P\Delta V + {W_e}^0)$. Here, ΔS indicates the molar entropy change in a unipolar reaction. Herein, the electrochemical work is written as ${W_e}^0$ when the electrochemical system is in equilibrium. In an isobaric process, if the electrochemical reaction is in progress, the electrochemical work is written as W_e; thus, the relationship of $Q = T\Delta S + W_e - {W_e}^0$ is obtained. In this case, Q is the heat absorbed when the electrochemical reaction is proceeding. We consider the current I and the heat dQ absorbed during time dt. Electrochemical work is the product of the potential difference (ΔE) and the electric charge (Idt); we denote the equilibrium potential of the cathode as E^0, and we hence obtain ${\Delta W_e}^0 = (E - E^0)Idt$. Here, we must add the following generation term, because the Joule heating effect and the heat exchange at the reaction interface cannot be ignored while the electrochemical reaction proceeds. Therefore, the heat absorbed at the single electrode/electrolyte interface dQ can be written as:

$$\frac{dQ}{dt} = \underbrace{\frac{T\Delta SI}{nF}}_{(entropy\ change)} \underbrace{+I^2R}_{(Joule\ heat)} \underbrace{-\eta I}_{(overpotential)} \underbrace{-q_t}_{(heat\ exchange)} \quad (9)$$

where n is the valence of ion, F is the Faraday constant, R is the electrode/electrolyte resistance ($\approx$ 0.4 Ω; as the electrolyte resistance [44]), η is the overpotential (= $E - E^0$; $E^0 = -1.6$ V), and q_t is the heat exchange between molten salt and electrode. Here, when C_p is given as the heat

capacity of the electrode, Q can be rewritten as follows:

$$\frac{dQ}{dt} = C_p \frac{dT}{dt} \tag{10}$$

From the $E = E_2$ region of the temperature–time curve of Fig. 2, the slope of the temperature change is approximated to a constant. Generally, q_t can be calculated by the following equation to assume the temperature difference between the WE and bath, ΔT $(= T_{WE} - T_{bath})$:

$$q_t = hA\Delta T \tag{11}$$

where h is the convective heat transfer coefficient, and A is the surface area of electrode. From the empirical formula of the Nusselt number, *Nu*, the heat transfer coefficient between a WE and bath is given by [45]:

$$Nu = \frac{hL}{k} \approx 2.0 \tag{12}$$

where $k(\approx 0.5\ \mathrm{Wm^{-1}K^{-1}})$ is the thermal conductivity of the bath [46] and L is the radius of the electrode. In the early stage of electrolysis, when *dQ*/*dt* can be assumed to be constant, we can analytically solve Eq. 9, and Fig. 9 shows the variations of the heat transfer in each term of Eq. 9 with potential. As the potential becomes significantly negative, the absolute values of all the terms increase, and the sum of the these corresponds to the temperature change of the WE. This result confirmed that the ΔS of Eq. 4 was positive. Liquid Ca deposition reaction does not occur spontaneously in the $CaCl_2$ melt, it is clearly $\Delta G > 0$. The enthalpy change can be given as $\Delta H = T\Delta S + \Delta G > 0$, and thus, the Ca deposition reaction in $CaCl_2$ melt is an endothermic reaction. Even in the electrolysis of the eutectic chloride melt, the metal deposition reactions are expected to be endothermic. Although ΔS in this

system is an unknown value, the apparent value can be estimated via the time integration of Eq. 5; each application of the potential in Ca precipitation gives the following equation (range of *t'*: 0–2 s):

$$\Delta S = \frac{1}{t'}\int_0^{t'} \frac{nF}{T_t I_t}\cdot\left(C_p\frac{dT}{dt} + {I_t}^2 R + \eta I_t + \frac{k\cdot Nu}{L}A\Delta T_t\right)dt \qquad (13)$$

Eq. 13 can be solved by numerical integration, and Fig. 10 shows the estimated apparent ΔS at each potential. It is almost zero for (a) E > -1.9 V; however, for (b) E < -2.0 V, it was estimated as a positive value and clearly shows an increasing trend. In Case (a), the effects of the second to fourth terms on the right side of Eq. 5 are considered to be relatively large. In Case (b), the ΔS value was 100–300 $JK^{-1}mol^{-1}$. By simulating Eq. 4 with the thermochemical software (FactSage7.0 was used for calculating the absolute entropy of Ca^{2+} in the melt, which was estimated with the help of approximations in aqueous solutions), we obtained $\Delta S = 18.6\,JK^{-1}mol^{-1}$ [47]. The experimental value was higher than the simulated value. This is probably because the simulated value is for an ideal system; on the other hand, the electrodeposited morphology of Ca in this system exhibits a unique dispersed phase. The excess energy was probably required to create the dispersed metal-and-salt interface and depends on the microscopic fog morphology [39, 40]. Unfortunately, no evidence has yet been obtained to support this hypothesis. The heat transport model represented in this section through the electrode/electrolyte interface is simplistic; it may be necessary to consider even smaller scale heat balances for a more detailed understanding. Further development toward precise micro-scale reaction models will be possible by combining in-situ observations with thermal analysis as proposed in this study.

Conclusions

We proposed a new method for direct measurement of electrochemical behavior in high-temperature molten salt by examining images of the electrode surface obtained by high-speed digital microscopy synchronized with thermal analysis. The advantage of this method is a direct detection in both of morphology and temperature. By applying this to a various molten chloride system, we estimated transient behavior of the electrodeposition pattern between liquid metal and impurity water by predicting the heat balance of cathode as followings.

In the case of the molten $CaCl_2$ single salt at 1173 K, the tendency of the temperature drop according to the applied potential was confirmed during Ca deposition despite the high current density. Furthermore, the entropy change at the time of Ca deposition was estimated by calculating the heat balance. In any composition of molten LiCl–KCl–$CaCl_2$ at 723–823 K, the temperature change of the cathode was relatively small when a negative potential was applied for liquid metal deposition, while significant heat generation was observed during the anodic dissolution reaction. Although a small amount of water was included in the system, the generated hydrogen may have decreased the purity of the Li or Ca-Li alloy electrodeposited on the cathode surface owing to hydride formation. The latter occurred because the measured heat absorption was much smaller than thermodynamically predicted. This reaction mechanism was supported by the high-speed direct observation of hydrogen gas and hydroxide generation on the electrode surface. Since this proposed scheme of synchronized

microscopy and thermoanalytical measurement can directly track the influence of impurities on interface phenomena, which are difficult to observe from the potential-current response in high-temperature molten salt, it is a useful method for understanding transport phenomena involving electrochemical reactions, even in high-temperature molten salt. In the future, by the development of thermal measurement sensitivity, it will be possible to clarify local transient behavior at the electrode interface.

Acknowledgments

This work was supported by the Grant-in-Aid for Scientific Research (KAKENHI) [grant number 18K14036 and 20H02491], Japan Society for the Promotion of Science; Takahashi Industrial and Economic Research Foundation [grant number H31-173]; Tanikawa Fund Promotion of Thermal Technology [H30-1]. We would especially like to thank Mr. Akihisa Ito of Tohoku University who designed the low-pass filter, amplifier devices, and improving of direct observation system. We would especially like to thank Mr. Hiromi Noguchi, Mr. Takumi Kaneko, and eco-processing laboratory members of Hokkaido University to discuss the electrochemical and thermodynamic experimental designing. We acknowledged Dr. Xu Gao and Prof. Shigeru Ueda of Tohoku university who supported thermodynamic analysis, provided direction, ideas, as well as suggestions to improve the paper. We would like to thank Mr. Tatsuya Ide, Dr. Koji Yasuda, and Prof. Toshiyuki Nohira of Kyoto University who designed the early versions of our special electrode.

References

[1] W. Kroll, *J. Electrochem. Soc.*, **78**, 35 (1940).

https://doi.org/10.1149/1.3071290.

[2] G. Z. Chen, D. J. Fray, and T. W. Farthing, *Nature*, **407**, 361 (2000).

https://doi.org/10.1038/35030069.

[3] K. Ono and R. O. Suzuki, *JOM*, **54**, 59 (2002).

https://doi.org/10.1007/BF02701078.

[4] R. O. Suzuki and S. Inoue, *Metall. Mater. Trans. B*, **34**, 277 (2003). https://doi.org/10.1007/s11663-003-0073-2.

[5] R. O. Suzuki, K. Ono, and K. Teranuma, *Metall. Mater. Trans. B*, **34**, 287 (2003). https://doi.org/10.1007/s11663-003-0074-1.

[6] H. Okamoto, Desk Handbook: Phase Diagrams for Binary Alloys, ASM International, Materials Park, OH, USA (2000).

[7] R. O. Suzuki, H. Noguchi, H. Hada, S. Natsui, and T. Kikuchi, *Mater. Trans.*, **58**, 341 (2017). https://doi.org/10.2320/matertrans.MK201625.

[8] Y. Sakamura, *J. Electrochem. Soc.*, **157**, E135 (2010).

https://doi.org/10.1149/1.3456631.

[9] J. -M. Hur, S. -C. Lee, S. -M. Jeong, and C. -S. Seo, *Chem. Lett.*, **36,** 1028 (2007). https://doi.org/10.1246/cl.2007.1028.

[10] S. M. Jeong, J. -Y. Jung, C. -S. Seo, and S. -W. Park, *J. Alloys Compd.*, **440**, 210 (2007). https://doi.org/10.1016/j.jallcom.2006.05.139.

[11] Y. Chen, Q. Xu, Q. Song, H. Li, Z. Ning, X. Lu, and D. J. Fray, *Electrochem. Commun.*, **64**, 1

(2016).

https://doi.org/10.1016/j.elecom.2015.12.015.

[12] K. Yasuda, T. Nohira, Y. H. Ogata, and Y. Ito, *J. Electrochem. Soc.*, **152**, D208 (2005). https://doi.org/10.1149/1.2042910.

[13] K. Yasuda, T. Nohira, Y. H. Ogata, and Y. Ito, *Electrochim. Acta*, **51,** 561 (2005). https://doi.org/10.1016/j.electacta.2005.05.014.

[14] D. S. M. Vishnu, N. Sanil, K. S. Mohandas, and K. Nagarajan, *J. Nucl. Mater.*, **470**, 179 (2016). https://doi.org/10.1016/j.jnucmat.2015.12.003.

[15] Z. Zhou, Y. Zhang, Y. Hua, P. Dong, C. Xu, Y. Li, and D. Wang, *Electrochim. Acta*, **271**, 490 (2018). https://doi.org/10.1016/j.electacta.2018.03.192.

[16] K. Liu, Y. Wang, Y. Di, and J. Peng, *Electrochim. Acta*, **318**, 236 (2019). https://doi.org/10.1016/j.electacta.2019.06.072.

[17] N. Suzuki, M. Tanaka, H. Noguchi, S. Natsui, T. Kikuchi, and R. O. Suzuki, *ECS Trans.*, **75,** 507 (2016).

https://doi.org/10.1149/07515.0507ecst.

[18] T. Matsuzaki, R. O. Suzuki, S. Natsui, T. Kikuchi, and M. Ueda, *Mater. Trans.*, **60**, 411 (2019). https://doi.org/10.2320/matertrans.MA201809.

[19] R. O. Suzuki, N. Suzuki, Y. Yashima, S. Natsui, and T. Kikuchi, Calciothermic Reduction and Electrolysis of Sulfides in $CaCl_2$ Melt, in: B. Davis et al. (Eds.) Extraction 2018. The Minerals, Metals & Materials Series, Springer, Cham, 2018, p. 763–771. https://doi.org/10.1007/978-3-319-95022-8_60.

[20] T. H. Okabe, R. O. Suzuki, T. Oishi, and K. Ono, *Mater. Trans.*, **32**, 485 (1991). https://doi.org/10.2320/matertrans1989.32.485.

[21] H. Noguchi, S. Natsui, T. Kikuchi, and R. O. Suzuki, *Electrochemistry*, **86,** 82 (2018). https://doi.org/10.5796/electrochemistry.17-00078.

[22] G. M. Haarberg, S. R. Johansen, J. Melaas, and R. Tunold, *Proc. – Electrochem. Soc.*, p. 449–456, (1990). https://doi.org/10.1149/199017.0449PV.

[23] G. M. Haarberg, *Proc. – Electrochem. Soc.*, p. 789–796, (2002). https://doi.org/10.1149/200219.0789PV.

[24] M. Ueda, Y. Abe, and T. Ohtsuka, *Mater. Lett.*, **60**, 635 (2006). https://doi.org/10.1016/j.matlet.2005.09.049.

[25] T. Takenaka, S. Akimura, and T. Morishige, *Electrochemistry*, **86**, 179 (2018). https://doi.org/10.5796/electrochemistry.17-00109.

[26] S. Natsui, T. Sudo, T. Kikuchi, and R. O. Suzuki, *Electrochem. Commun.*, **81**, 43 (2017). https://doi.org/10.1016/j.elecom.2017.06.001.

[27] S. Natsui, T. Sudo, T. Kaneko, K. Tonya, D. Nakajima, T. Kikuchi, and R.O. Suzuki, *Sci. Rep.*, **8**, 13114 (2018). https://doi.org/10.1038/s41598-018-31521-3.

[28] J. N. Agar, Thermogalvanic cells. In P. Delahay (Ed.): Advances in Electrochemistry and Electrochemical Engineering, Vol. 3., p. 31-121, Interscience Publishers, London (1963).

[29] K. R. Bickel, K. D. Etzel, V. Halka, and R. Schuster, *Electrochimica Acta*, **112,** , 801 (2013). https://doi.org/10.1016/j.electacta.2013.06.056

[30] Y. V. Kuz'minskii and A. A. Andriiko, *J. Electroanal. Chem. and Interfac. Electrochem.*, **252**, 39 (1988). https://doi.org/10.1016/0022-0728(88)85069-1.

[31] T. Ozeki, N. Ogawa, K. Aikawa, I. Watanabe, and S. Ikeda, *J. Electroanal. Chem. and Interfac. Electrochem.*, **145**, 53 (1983). https://doi.org/10.1016/S0022-0728(83)80293-9.

[32] Y. Kashiwaya, C. E. Cicutti, A. W. Cramb, and K. Ishii, *ISIJ Int.*, **38**, 348 (1998). https://doi.org/10.2355/isijinternational.38.348.

[33] H. Takebe, Y. Takahashi, and T. Okura, *J. Sustainable Metall.*, **5**, 210 (2019). https://doi.org/10.1007/s40831-019-00211-3.

[34] L. Zhang, and W. Wang, *ISIJ Int.*, **59**, 1041 (2019).

https://doi.org/10.2355/isijinternational.ISIJINT-2018-560.

[35] T. B. Massalski, H. Okamoto, P. R Subramanian, and L. Kacprzak (Eds.), Binary Alloy Phase Diagrams, 2nd ed., p. 2446–2447, ASM International, Materials Park, OH, USA, (1990).

[36] A. J. Bard and L. R. Faulkner, Electrochemical Methods — Fundamentals and Applications, 2nd Ed., Wiley, New York, chapter 1, (2001).

https://doi.org/10.1023/A:1021637209564

[37] N. J. Gese and B. Pesic, Electrochemistry of LiCl-Li_2O-H_2O molten salt systems (No. INL/CON-12-26774). Idaho National Laboratory (INL), (2013).

[38] N. Watanabe, K. Nakanishi, and T. Nakajima, *Nippon Kagaku Kaishi*, **1974**, 401 (1974). https://doi.org/10.1246/nikkashi.1974.401.

[39] A. Merwin, W. C. Phillips, M. A. Williamson, J. L. Willit, P. N. Motsegood, and D. Chidambaram, *Sci. Rep.*, **6**, 25435 (2016). https://doi.org/10.1038/srep25435 (2016).

[40] J. Guo, A. Merwin, C. J. Benmore, Z. G. Mei, N. C. Hoyt, and M. A. Williamson, *J. Phys. Chem. B*, **123**, 10036 (2019). https://doi.org/10.1021/acs.jpcb.9b07479

[41] Y. Maeda and A. Katsuta, *Bull. Chem. Soc. Jpn.*, **67**, 575 (1994). https://doi.org/10.1246/bcsj.67.575.

[42] Y. Maeda and T. Kumagai, *Thermochim. Acta*, **267,** 139, (1995) https://doi.org/10.1016/0040-6031(95)02473-5.

[43] A. J. DeBethune, *J. Electrochem. Soc.*, **106**, 616, (1959) https://doi.org/10.1149/1.2427448

[44] G. J. Janz, R. P. T. Tomkins, C. B. Allen, J. R. Downey Jr., G. L. Garner, U. Krebs, and S. K. Singer, *J. Phys. Chem. Ref. Data*, **4**(4), 962 (1975).

[45] W. E. Ranz and W. R. Marshall, *Chem. Eng. Prog.*, **48**, 141 (1952).

[46] Y. Nagasaka, N. Nakazawa, and A. Nagashima, *Int. J. Thermophys.*, **13,** 555 (1992). https://doi.org/10.1007/BF00501941.

[47] C. W. Bale, E. Bélisle, P. Chartrand, S.A. Decterov, G. Eriksson, A.E. Gheribi, K. Hack, I.-H. Jung, Y.-B. Kang, J. Melançon, A.D. Pelton, S. Petersen, C. Robelin, J. Sangster, P. Spencer, and M-A. Van Ende, Reprint of: FactSage thermochemical software and databases, 2010–2016. Calphad, 55 (2016), 1-19. https://doi.org/10.1016/j.calphad.2016.07.004.

Figure captions

Fig. 1. Schematic diagrams of the experimental setup. (a) Experimental apparatus. Black, red, and blue lines show wiring related to electrolysis, high-speed imaging, and thermal measurement, respectively. (b) Mo sheath thermocouple electrode.

Fig. 2. Time-dependent changes of current density and temperature in $CaCl_2$ melt measured by a thermocouple implanted in the Mo tube electrode. The bath temperature was fixed at 1173 K. The applied potential was varied from -1.6 to -2.7 V vs. Ag^+/Ag.

Fig. 3. Photographs of the electrodeposited melt and black colloidal metal formed on the Mo tube electrode at 1173 K. The applied potential was varied from -1.7, -2.1 and -2.6 V vs. Ag^+/Ag.

Fig. 4. Time-dependent changes of the current density and temperature in each eutectic mixture measured by a thermocouple implanted in the Mo tube electrode. The bath temperature was fixed at 823 K in (a)–(d). The applied potential was (a) -2.4, (b) -2.5, (c) -2.6, and (d) -2.7 V vs. Ag^+/Ag.

Fig. 5. Time-dependent changes of the current density and temperature in each eutectic mixture measured by a thermocouple implanted in the Mo tube electrode. The bath temperature was varied from 723 to 823 K, and the applied potential was fixed at -2.7 V.

Fig. 6. Influence of applied potential and chloride composition on the macroscopic morphology of the electrodeposited metal.

Fig. 7. Change in current efficiency at each potential.

Fig. 8. Current-temperature-time curves and macroscopic morphology of electrodeposited in hygroscopic LiCl–$CaCl_2$ (E_2 = -3.0 V vs. Ag^+/Ag, bath temperature = 823 K).

Fig. 9. Effects of various factors contributing to the heat transfer for the working electrode (WE) in each potential.

Fig. 10. Potential dependence of the molar entropy change of Ca electrodeposition from $CaCl_2$ melt at 1173 K due to electrochemical reaction estimated from thermal measurements.

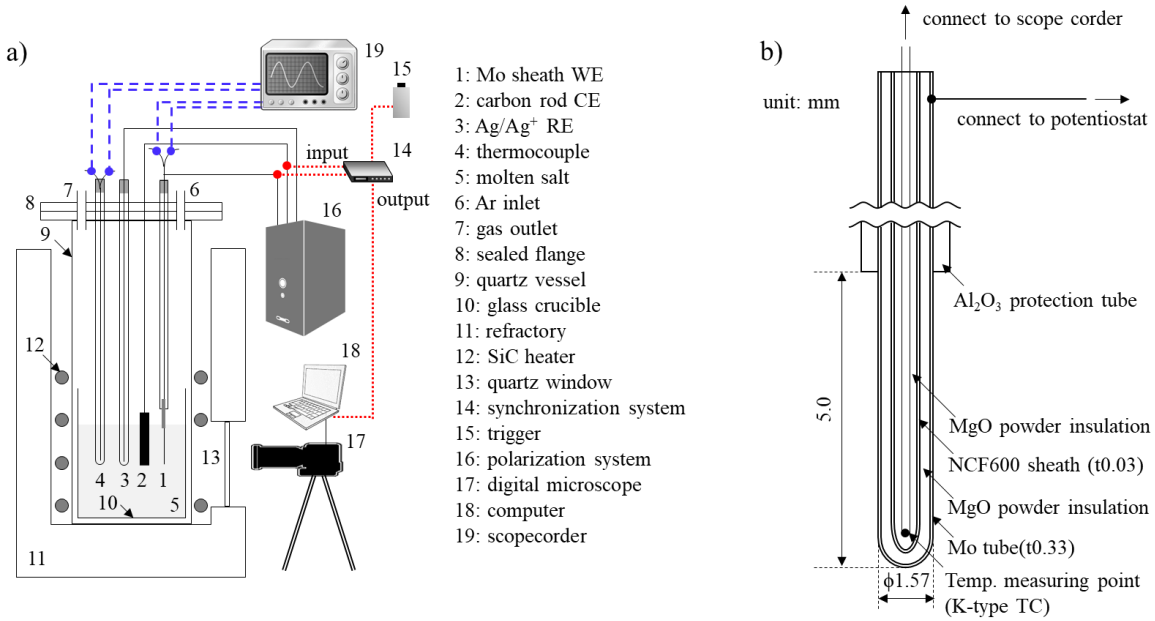
a)
b)
input
output
connect to scope corder
unit: mm
connect to potentiostat
Al_2O_3 protection tube
5.0
MgO powder insulation
NCF600 sheath (t0.03)
MgO powder insulation
Mo tube(t0.33)
ϕ1.57
Temp. measuring point
(K-type TC)
1: Mo sheath WE
2: carbon rod CE
3: Ag/Ag^+ RE
4: thermocouple
5: molten salt
6: Ar inlet
7: gas outlet
8: sealed flange
9: quartz vessel
10: glass crucible
11: refractory
12: SiC heater
13: quartz window
14: synchronization system
15: trigger
16: polarization system
17: digital microscope
18: computer
19: scopecorder

Figure 1

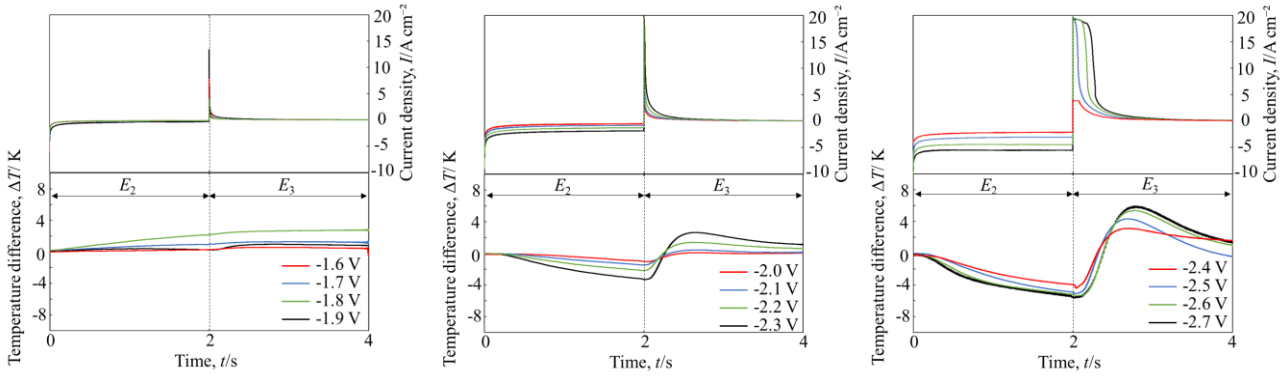
Temperature difference, ΔT/ K
Current density, I/A cm⁻²
E2
E3
-1.6 V
-1.7 V
-1.8 V
-1.9 V
-2.0 V
-2.1 V
-2.2 V
-2.3 V
-2.4 V
-2.5 V
-2.6 V
-2.7 V
Time, t/s

Figure 2

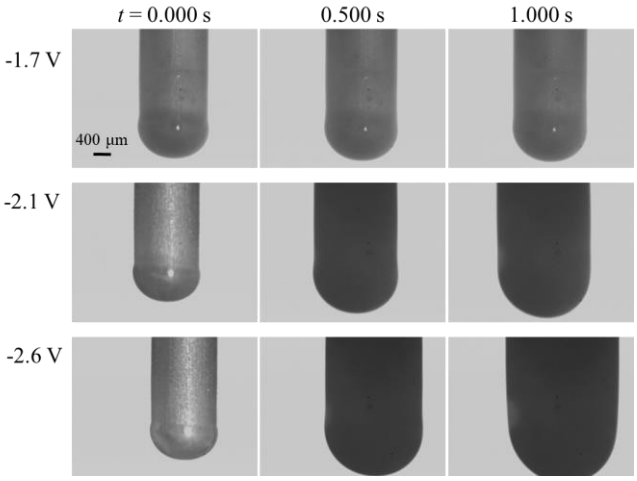

Figure 3

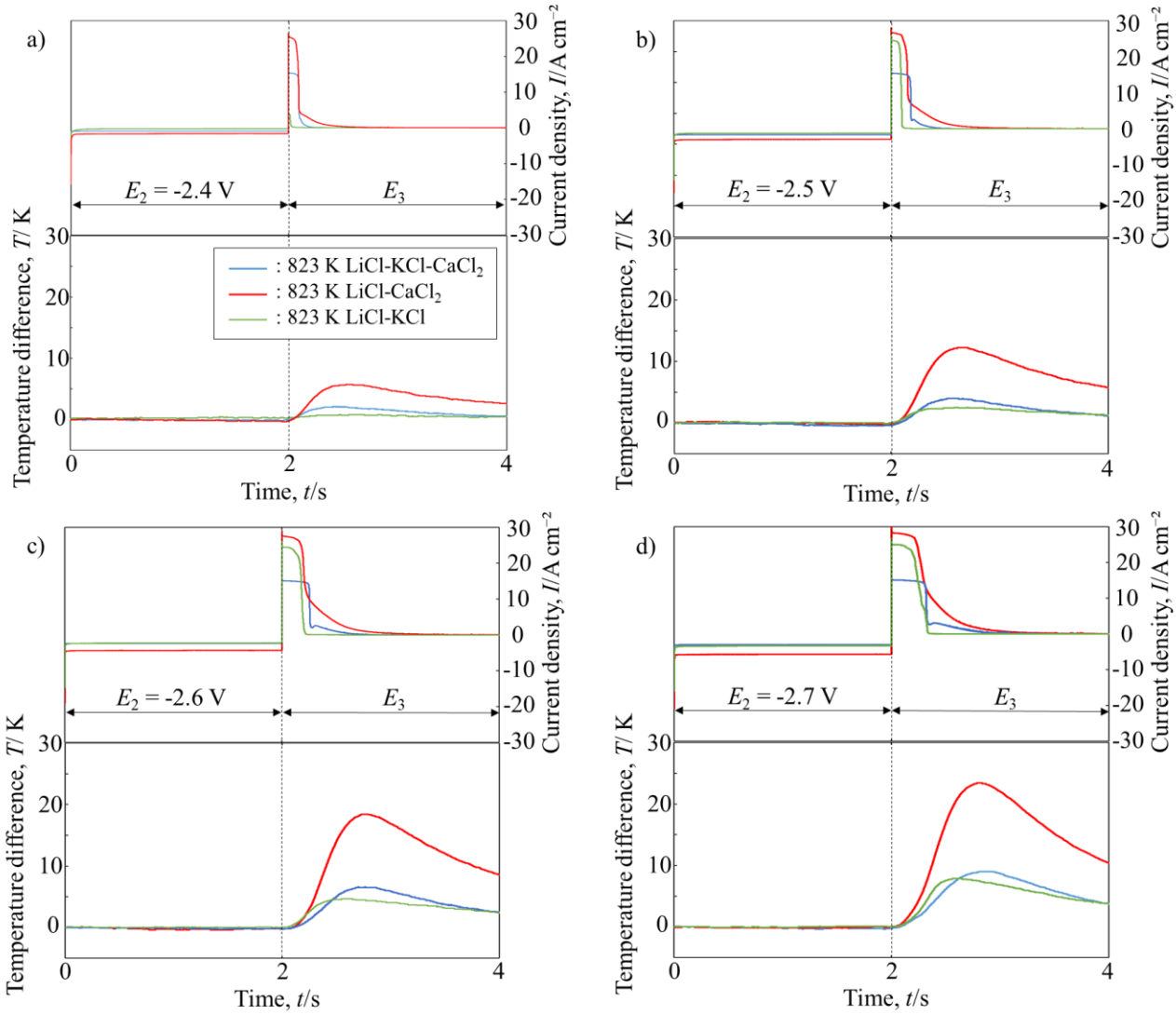
a)
b)
c)
d)
E_2 = -2.4 V
E_2 = -2.5 V
E_2 = -2.6 V
E_2 = -2.7 V
E_3
: 823 K LiCl-KCl-$CaCl_2$
: 823 K LiCl-$CaCl_2$
: 823 K LiCl-KCl
Temperature difference, T/ K
Current density, I/A cm^{-2}
Time, t/s

Figure 4

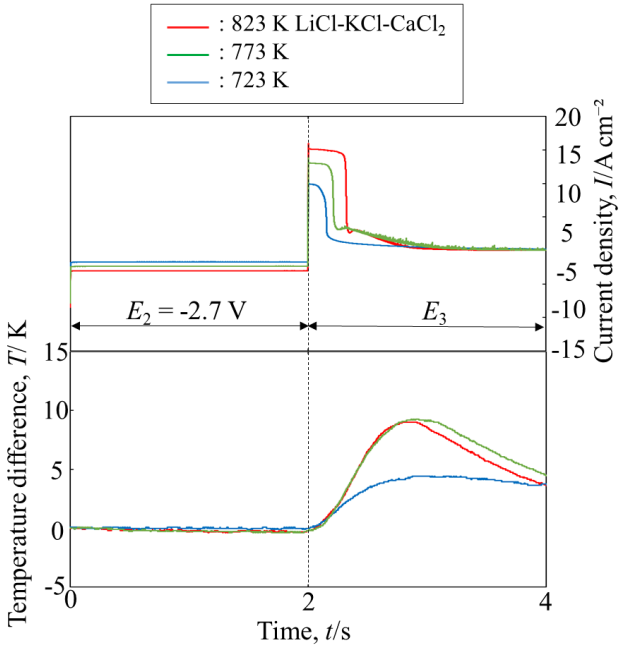
: 823 K LiCl-KCl-CaCl2
: 773 K
: 723 K
E2 = -2.7 V
E3
Temperature difference, T/ K
Current density, I/A cm−2
Time, t/s
20
15
10
5
-5
-10
-15
15
10
5
0
-5
0
2
4

Figure 5

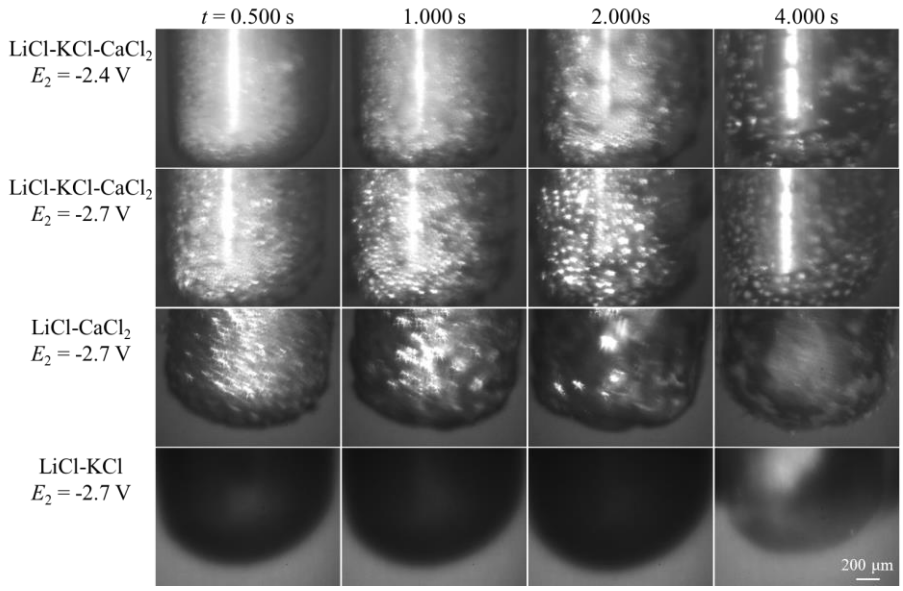
t = 0.500 s
1.000 s
2.000s
4.000 s
LiCl-KCl-CaCl2
E2 = -2.4 V
LiCl-KCl-CaCl2
E2 = -2.7 V
LiCl-CaCl2
E2 = -2.7 V
LiCl-KCl
E2 = -2.7 V
200 μm

Figure 6

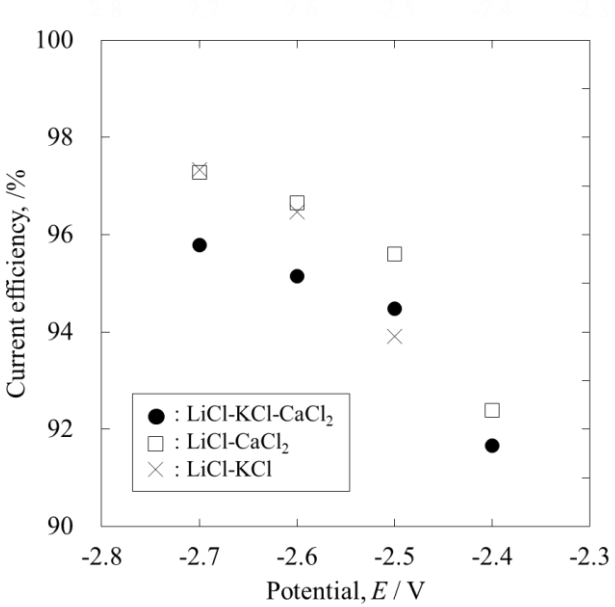
100
98
96
94
92
90
Current efficiency, /%
-2.8
-2.7
-2.6
-2.5
-2.4
-2.3
Potential, E / V
● : LiCl-KCl-CaCl2
□ : LiCl-CaCl2
× : LiCl-KCl

Figure 7

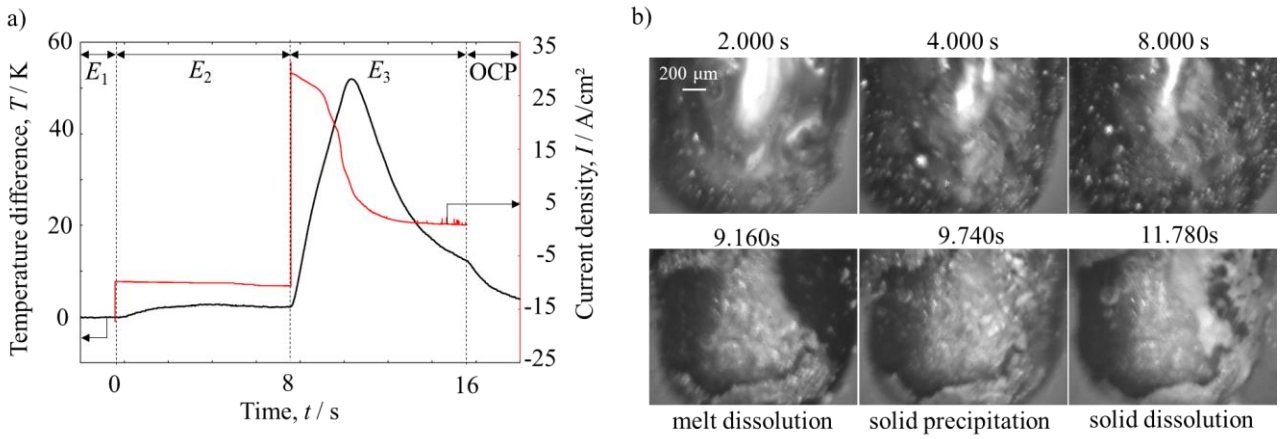
a)
Temperature difference, T / K
Current density, I / A/cm²
E1
E2
E3
OCP
Time, t / s
b)
2.000 s
4.000 s
8.000 s
200 µm
9.160s
9.740s
11.780s
melt dissolution
solid precipitation
solid dissolution

Figure 8

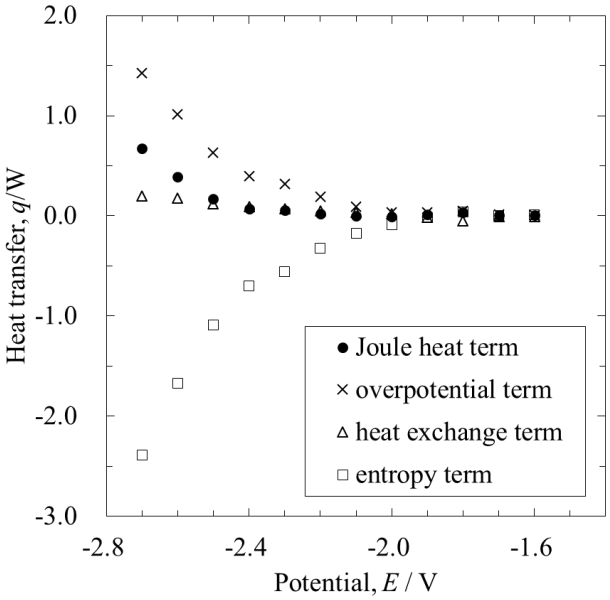
2.0
1.0
0.0
-1.0
-2.0
-3.0
-2.8
-2.4
-2.0
-1.6
Heat transfer, q/W
Potential, E / V
Joule heat term
overpotential term
heat exchange term
entropy term

Figure 9

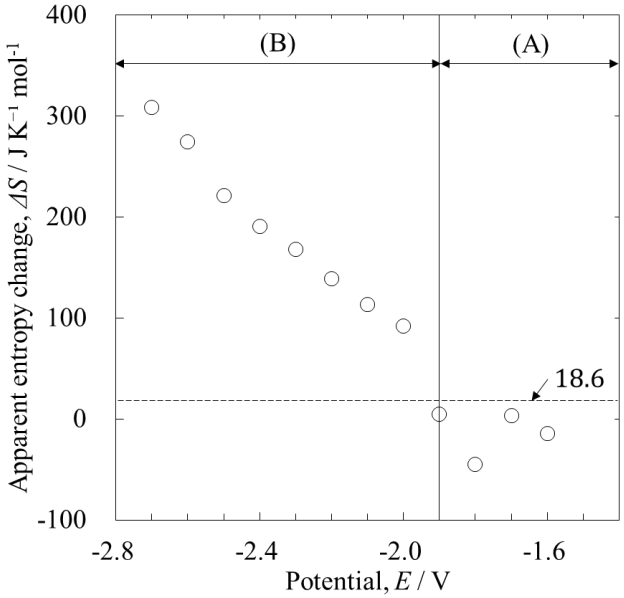
400
300
200
100
0
-100
(B)
(A)
18.6
-2.8
-2.4
-2.0
-1.6
Apparent entropy change, ΔS / J K⁻¹ mol⁻¹
Potential, E / V

Figure 10